

ON THE DIFFUSE $\text{Ly}\alpha$ HALO AROUND $\text{Ly}\alpha$ EMITTING GALAXIESETHAN LAKE¹, ZHENG ZHENG¹, RENYUE CEN², RAPHAEL SADOUN¹, RIEKO MOMOSE³, AND MASAMI OUCHI^{3,4}¹ Department of Physics and Astronomy, University of Utah, 115 South 1400 East, Salt Lake City, UT 84112, USA;

ethan.lake@utah.edu, zhengzheng@astro.utah.edu

² Princeton University Observatory, Princeton, NJ 08544, USA³ Institute for Cosmic Ray Research, The University of Tokyo, 5-1-5 Kashiwanoha, Kashiwa, Chiba 277-8583, Japan⁴ Kavli Institute for the Physics and Mathematics of the Universe (WPI), The University of Tokyo, 5-1-5 Kashiwanoha, Kashiwa, Chiba 277-8583, Japan

Received 2015 February 2; accepted 2015 April 8; published 2015 June 5

ABSTRACT

$\text{Ly}\alpha$ photons scattered by neutral hydrogen atoms in the circumgalactic media or produced in the halos of star-forming galaxies are expected to lead to extended $\text{Ly}\alpha$ emission around galaxies. Such low surface brightness $\text{Ly}\alpha$ halos (LAHs) have been detected by stacking $\text{Ly}\alpha$ images of high-redshift star-forming galaxies. We study the origin of LAHs by performing radiative transfer modeling of nine $z = 3.1$ $\text{Ly}\alpha$ emitters (LAEs) in a high resolution hydrodynamic cosmological galaxy formation simulation. We develop a method of computing the mean $\text{Ly}\alpha$ surface brightness profile of each LAE by effectively integrating over many different observing directions. Without adjusting any parameters, our model yields an average $\text{Ly}\alpha$ surface brightness profile in remarkable agreement with observations. We find that observed LAHs cannot be accounted for solely by photons originating from the central LAE and scattered to large radii by hydrogen atoms in the circumgalactic gas. Instead, $\text{Ly}\alpha$ emission from regions in the outer halo is primarily responsible for producing the extended LAHs seen in observations, which potentially includes both star-forming and cooling radiation. With the limit on the star formation contribution set by the ultraviolet halo measurement, we find that cooling radiation can play an important role in forming the extended LAHs. We discuss the implications and caveats of such a picture.

Key words: cosmology: observations – galaxies: high-redshift – intergalactic medium – radiative transfer – scattering

1. INTRODUCTION

The $\text{Ly}\alpha$ line is an important cosmological tool for studying star-forming galaxies in the young universe, and has been found to aid in the detection of high-redshift galaxies (Rhoads et al. 2003; Gawiser et al. 2007; Ouchi et al. 2008; Guaita et al. 2010). As ionizing photons are emitted from young stars, they ionize neutral hydrogen in the surrounding interstellar medium (ISM), and are likely to be re-emitted as $\text{Ly}\alpha$ photons following recombination (Partridge & Peebles 1967). After they escape the ISM surrounding their parent stars, they are predicted to undergo resonant scattering with neutral hydrogen gas in the surrounding medium as a result of the radiative transfer process, diffusing out both spatially and in frequency (Zheng et al. 2011a). As such, extended halos of neutral hydrogen around these $\text{Ly}\alpha$ emitters (LAEs) are predicted to be illuminated by scattered $\text{Ly}\alpha$ photons.

Many theoretical studies have predicted the existence of these so-called $\text{Ly}\alpha$ halos (LAHs) around high-redshift galaxies (e.g., Tasitsiomi 2006; Laursen & Sommer-Larsen 2007; Dijkstra & Loeb 2009; Laursen et al. 2009; Barnes & Haehnelt 2010; Zheng et al. 2010, 2011a; Barnes et al. 2011). While these LAHs are predicted to generally be too faint to be detected on an individual basis at $z \geq 2$, their presence can be revealed by stacking tens to hundreds of narrow band images of high-redshift LAEs (Fynbo et al. 2003; Steidel et al. 2011; Zheng et al. 2011a; Matsuda et al. 2012; Momose et al. 2014). Although observationally there seems to be a consensus in favor of their existence, there are also reports of null detections of LAHs. Feldmeier et al. (2013) find marginal evidence and no evidence of LAHs for $z \sim 3.1$ and $z \sim 2.1$ LAEs, while Jiang et al. (2013) find evidence of LAHs based on results using stacked images of LAEs at redshifts of 5.7 and

6.6. Such contradicting results may be caused by small number statistics or unknown systematics (Momose et al. 2014).

The shape and size of LAHs can yield insights into the spatial distribution and kinematic properties of the circumgalactic and intergalactic medium (IGM) surrounding LAEs (Zheng et al. 2011a). The shape can also be used to constrain cosmic reionization, with reionization leading to steeper surface brightness profiles (Jeeson-Daniel et al. 2012). Detailed theoretical studies of LAHs can help in understanding their origin and properties.

The aim of this paper is to apply a Monte Carlo radiative transfer code (Zheng & Miralda-Escudé 2002) to study diffuse LAHs surrounding $z \sim 3.1$ star-forming galaxies in a high-resolution galaxy formation simulation. By comparing with observational data, we hope to gain insight about the origin and composition of these diffuse LAHs.

This paper is divided into several sections. In Section 2, we describe the modeling method and the construction of the average $\text{Ly}\alpha$ surface brightness profile for each model LAE. Our main analyses and results are presented in Section 3, with comparisons to observations and a discussion of possible constraints imposed by the profile in the ultraviolet (UV) band. Finally, we summarize our results and discuss the implications in Section 4.

2. MODEL

2.1. $\text{Ly}\alpha$ Radiative Transfer Modeling of Simulated Star-forming Galaxies

Our $\text{Ly}\alpha$ radiative transfer modeling of simulated star-forming galaxies is based on a cosmological simulation with the adaptive mesh refinement Eulerian hydro code Enzo (Bryan & Norman 2000; Joung et al. 2009), as detailed in Cen (2012)

and Cen & Zheng (2013). In brief, a region of comoving size $21 \times 24 \times 20 h^{-3} \text{ Mpc}^3$ in a low-resolution simulation (with a box size of $120 h^{-1} \text{ Mpc}$ comoving on a side) is chosen to be resimulated at high resolution. The resimulation has a dark matter particle mass of $1.3 \times 10^7 h^{-1} M_\odot$ and the mesh refinement ensures a spatial resolution better than $111 h^{-1} \text{ pc}$ (physical). The resimulation includes an ionizing UV background and the self-shielding of the gas, metallicity-dependent radiative cooling, molecular hydrogen formation, star formation, and supernova feedback. The mass of a star particle is typically $\sim 10^6 M_\odot$. The simulation assumes a spatially flat Λ cold dark matter model with the following cosmological parameters: $\Omega_m = 0.28$, $\Omega_b = 0.046$, $H_0 = 100h \text{ km s}^{-1} \text{ Mpc}^{-1}$ with $h = 0.70$, $\sigma_8 = 0.82$, and $n_s = 0.96$.

The simulation has been used to study the kinematic properties traced by unsaturated metal lines in damped Ly α systems (DLAs), which is in good agreement with observations (Cen 2012). The simulation has also been applied to study the partition of stellar light into optical and infrared light (Cen 2011). In Cen & Zheng (2013), a model of Ly α blobs (LABs) is developed based on Ly α radiative transfer modeling of the simulated star-forming galaxies in massive halos, and the observed relation between Ly α luminosity and LAB size and LAB luminosity function at $z \sim 3.1$ have been successfully reproduced. In this paper, we select from the simulation nine $z = 3.1$ star-forming galaxies in halos of mass $10^{11.5} M_\odot$ to study the properties of LAHs associated with them. The value of $10^{11.5} M_\odot$ is chosen as a starting point for our analysis, and is within current constraints on LAE halo mass of $10^{11 \pm 1} M_\odot$ (Ouchi et al. 2010). The mean stellar mass of these nine galaxies is about $2.9 \times 10^{10} M_\odot$.

We implement a Monte Carlo code developed by Zheng & Miralda-Escudé (2002) for the Ly α radiative transfer calculation in extended neutral hydrogen distributions surrounding our simulated LAEs. This code has been applied to study LAEs and LABs (e.g., Zheng et al. 2010, 2011a, 2011b; Cen & Zheng 2013; Zheng & Wallace 2014). For each galaxy, we store the relevant quantities from the simulation in a uniform cubic grid of $4R_{\text{vir}}$ on a side, with cell size 319 pc (physical, corresponding to $0''.04$). Here R_{vir} is the virial radius of the host halo, which is on average $\sim 56 \text{ kpc}$ (physical) for the nine $10^{11.5} M_\odot$ halos we consider. The quantities include the Ly α luminosity, neutral hydrogen density, temperature, and velocity. The Ly α luminosity is separated into star formation and cooling contributions. The Ly α luminosity from star formation is computed as $L_{\text{Ly}\alpha} = 10^{42} [\text{SFR}/(M_\odot \text{ yr}^{-1})] \text{ erg s}^{-1}$ (Furlanetto et al. 2005), where SFR is the star formation rate in the cell. The Ly α luminosity from cooling radiation is computed from the de-excitation rate, which depends on neutral hydrogen density and temperature that are computed self-consistently by following the relevant species in a non-equilibrium fashion.

Each photon launched from a cell is assigned a weight, calculated by dividing the total Ly α luminosity of the cell by the number of simulation photons launched from it. Such cell-dependent weights are accounted for in computing the Ly α surface brightness profiles. The scatterings of the photon with neutral hydrogen atoms on its way out and the corresponding changes in position, direction, and frequency are tracked until it escapes the grid boundary. We record the initial position of each photon, the position of the last scattering, the direction and frequency after the last scattering, and the fractional

contribution of cooling radiation to its total luminosity. This information is used to compute a mean surface brightness profile for each LAE, averaged over all directions (see Section 2.2).

At each scattering, we also compute the escape probability toward a fixed direction and collect the escaping Ly α photons onto an integral-field-unit-like three-dimensional (3D) array with pixel size the same as the cell size, which allows us to construct a Ly α image of each LAE as viewed along the chosen direction (Zheng & Miralda-Escudé 2002).

Finally, we account for the effects of the IGM outside of the box and the ISM in star-forming regions on Ly α emission, following the approximate methods in Cen & Zheng (2013).

In brief, for each photon escaping the box at frequency ν , we calculate the scattering optical depth τ_ν from the edge of the box to an observer at $z = 0$ using the redshift-dependent IGM hydrogen density and apply a factor of $e^{-\tau_\nu}$ correction for the IGM absorption. While such a correction neglects the differences in the IGM along different directions, it serves our purpose of introducing an overall average effect of the IGM. We also apply an effective ISM dust attenuation to the intrinsic Ly α emission by multiplying the luminosity represented by each simulation photon by a simple $e^{-\tau}$ factor, with $\tau = 0.2 [\text{SFR}/(M_\odot \text{ yr}^{-1})]^{0.6}$. This is loosely motivated by the observational trends of higher dust attenuation in galaxies with higher SFR (Brinchmann et al. 2004; Zahid et al. 2013), and the power-law index follows the slope of the metal column density dependence on SFR in the simulation. The dust extinction can be thought as applied to the ionizing photons around the H II regions, lowering the luminosity of Ly α emission converted from ionizing photons through recombination. The factor is also intended to absorb uncertainties in the galaxy formation simulation (e.g., in the predicted SFR). Our methods of applying IGM and ISM absorption are the same as adopted in Cen & Zheng (2013), in which the LAB luminosity function and luminosity–size relation have been successfully reproduced, suggesting that the approximate treatments work well in capturing the major IGM and ISM effects and in absorbing model uncertainties. In our current work of LAHs, we do not adjust any parameters and simply use the direct outputs of the radiative transfer model to compare to observations.

We show in Figure 1 the column density distribution of neutral hydrogen gas around each of our model LAEs, viewed from a fixed direction. The black contour curves are drawn at $10^{20.3} \text{ cm}^{-2}$, delineating regions corresponding to DLAs. DLAs represent regions extremely opaque to Ly α photons, while Ly α photons can be significantly scattered in regions of much lower column densities (e.g., above 10^{15} cm^{-2}). The images reveal extended, filamentary structures of neutral hydrogen connecting regions of high column densities. Scatterings of Ly α photons off hydrogen atoms in these structures leave signatures in the resulting Ly α surface brightness distributions.

Figure 2 shows the corresponding Ly α images of the nine LAEs in our analysis. The isophotal contours in each image correspond to $10^{-17} \text{ erg s}^{-1} \text{ cm}^{-2} \text{ arcsec}^{-2}$, about the surface brightness threshold for detecting individual $z \sim 3.1$ LAEs (Ouchi et al. 2008). These images reveal a rich degree of structures and a variety of morphologies at fainter surface brightness levels, which allows the LAHs to be revealed by the stacking analysis. The surface brightness distribution depends on the viewing angle (e.g., Zheng et al. 2010). The stacked

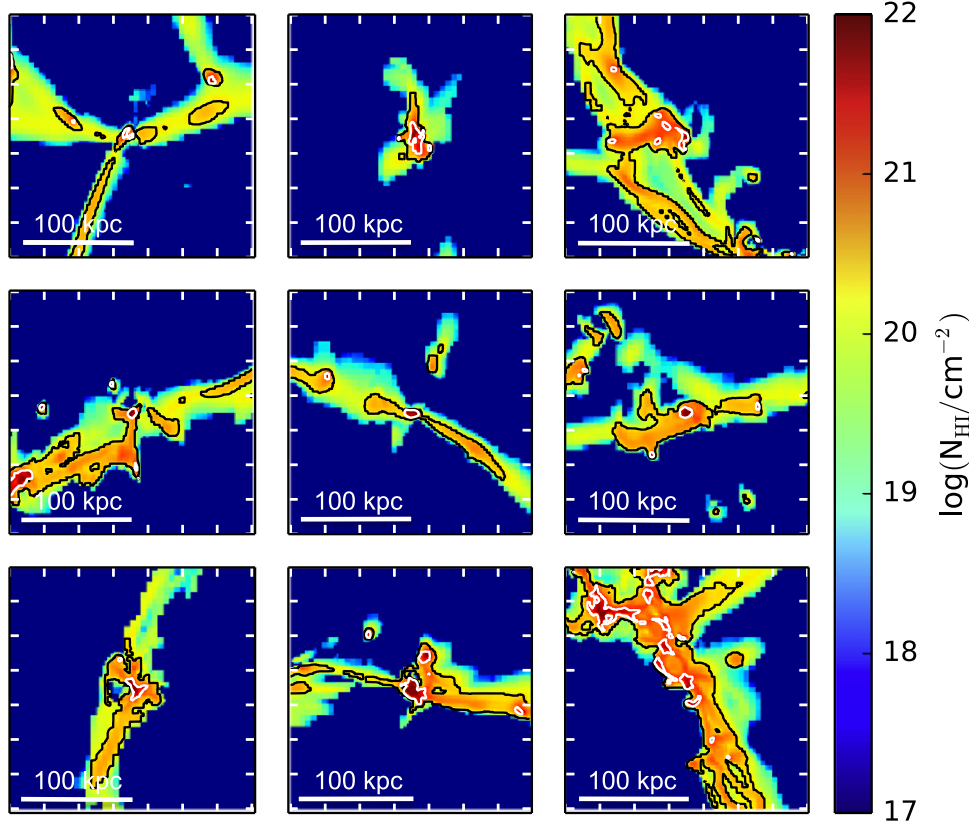


Figure 1. Neutral hydrogen column density maps for the model LAEs in our analysis. Each image is 224 kpc (physical) on a side. The column density is computed by integrating over the whole box along the line of sight (224 kpc physical). The black contours are drawn at $10^{20.3} \text{ cm}^{-2}$, within which are regions corresponding to DLAs. The white contours are drawn at $10^{21.3} \text{ cm}^{-2}$. Extended filamentary structures of neutral hydrogen are seen, which are connected to the extended Ly α emission discussed in this paper.

image (as in Momose et al. 2014) for a sample of LAEs comes from averaging many images from galaxies of random orientations. For the relatively small number of galaxies modeled here, we can form the mean surface brightness distribution by viewing each galaxy from many different observing directions.

2.2. Computing the Mean Ly α Surface Brightness Profiles of Model LAEs

First, let us consider an observer located along a direction \mathbf{k} from one of our model galaxies. The average surface brightness $\text{SB}(\mathbf{R}, \mathbf{k})$ at a projected radius R (physical) to the galaxy center as seen by the observer can be computed as (assuming a spatially flat universe)

$$\text{SB}(\mathbf{R}, \mathbf{k}) = \frac{\Delta L (1+z)^{-2}}{\Delta \Omega D_c^2 [A(1+z)^2/D_c^2]}, \quad (1)$$

where $\Delta \Omega$ is a small solid angle centered around \mathbf{k} , $A \equiv 2\pi R \Delta R$ is the area of a small annulus around R , and ΔL is the total luminosity of escaped Ly α photons falling into $\Delta \Omega$ and with projected last scattering position within A . The quantity $\Delta L (1+z)^{-2}/(\Delta \Omega D_c^2)$ is the corresponding flux ($\text{erg s}^{-1} \text{ cm}^{-2}$) the observer at a comoving distance D_c receives, with the two factors of $1+z$ from energy redshift and time dilation. The quantity $A(1+z)^2/D_c^2$ is the solid angle

extended by the annulus, seen by the observer, with the $(1+z)^2$ factor converting physical area to comoving.

The surface brightness profile at projected radius R averaged over all observing directions is then

$$\langle \text{SB}(R) \rangle = \frac{1}{4\pi} \int \text{SB}(\mathbf{R}, \mathbf{k}) d\Omega. \quad (2)$$

Given Equation (1), for the annulus at a given R and ΔR , we only need to obtain the average of $\Delta L/\Delta \Omega$ over all observing directions for computing the integral in Equation (2). Denoting the total Ly α luminosity from this annulus as L_A , we then have $L_A = \int \Delta L/\Delta \Omega d\Omega$. In the limit of an infinite number of observing directions, we obtain

$$\langle \text{SB}(R) \rangle = \frac{L_A}{4\pi A (1+z)^4}. \quad (3)$$

This equation is the basis of computing the mean Ly α surface brightness profile for each model LAE, along with the information we record for the escaping Ly α photons. For the mean Ly α surface brightness at projected radius R , instead of producing images viewed from many directions, we only need to obtain the sum of the total Ly α luminosity L_A for photons whose projected radii fall into the annulus around R ($R \pm \Delta R/2$ with an area A). The projected radius R_γ of a photon is computed from its escaping direction \mathbf{k}_γ and its position of last scattering \mathbf{r}_s (with respect to the galaxy center) as

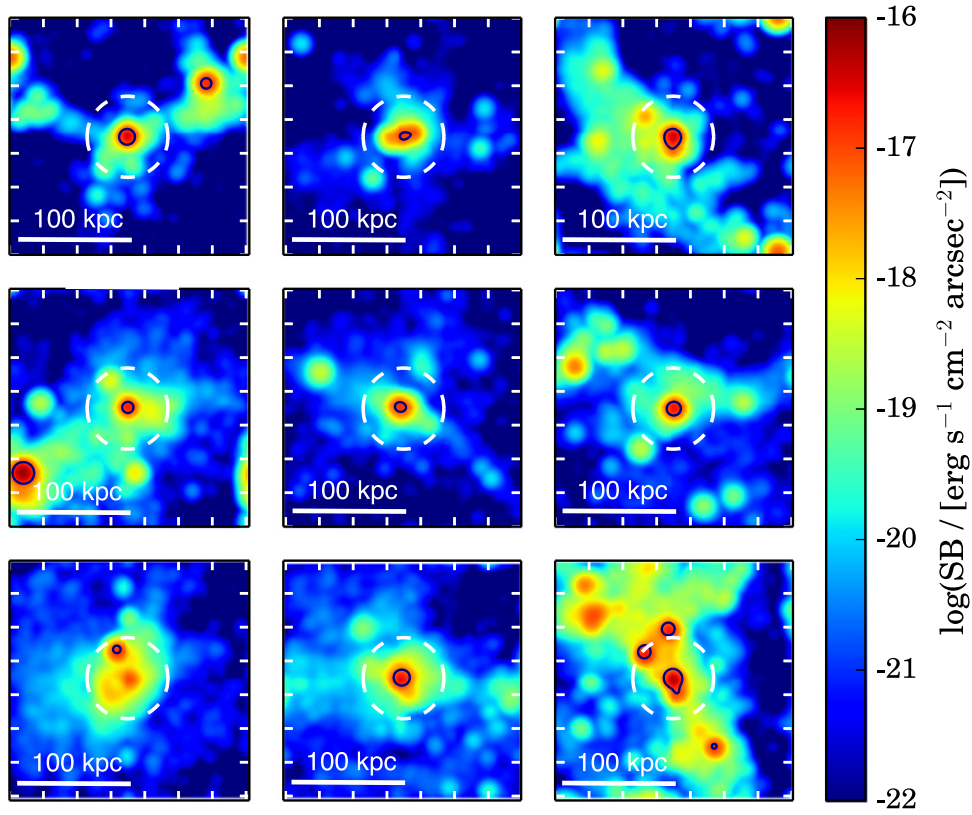


Figure 2. Ly α surface brightness images for all nine model LAEs in our analysis. Each image is 224 kpc (physical) on a side and has been smoothed by a 2D Gaussian kernel with a FWHM of $1''.32$ to match the observation setup. Isophotal contours are drawn in black at the limit of observational detection, $10^{-17} \text{ erg s}^{-1} \text{ cm}^{-2} \text{ arcsec}^{-2}$. The dashed circle in each panel has a radius of 40 kpc, beyond which the systematic effects in the image stacking analysis in Momose et al. (2014) start to become important. The images show a rich diversity in structure at surface brightness levels below the detection threshold, which contributes to the extended LAHs.

$R_\gamma = \sqrt{r_{\text{ls}}^2 - (\mathbf{k}_\gamma \cdot \mathbf{r}_{\text{ls}})^2}$. We have verified that the method gives the same results as that from averaging images over many observational directions.

Our simulation has a much higher resolution (cell size of $\sim 0''.04$) than the observation in Momose et al. (2014). To mimic the smoothing effect in the images of Momose et al. (2014), we obtain the final surface brightness profile by convolving the resulting Ly α image with a 2D Gaussian kernel with a FWHM of $1''.32$, corresponding to 10.3 kpc (physical) at $z = 3.1$.

3. RESULTS

We first present the results on the mean Ly α surface brightness profile in our model. We then decompose the mean profile in various ways to study its origin. Finally, we compare our UV profile to observations in order to further constrain the relative contributions of cooling and star-forming emission.

3.1. The Mean Ly α Surface Brightness Profile

The left panel of Figure 3 shows the mean surface brightness profiles from the smoothed images of the nine model LAEs in our analysis. The overall mean of the nine profiles is plotted in black. For each LAE, the central profile (e.g., $R \lesssim 15$ kpc) is largely determined by the smoothing kernel (point-spread function; PSF). The peak surface brightness at the center shows a small variation among the nine individual profiles, around $(1-3) \times 10^{-17} \text{ erg s}^{-1} \text{ cm}^{-2} \text{ arcsec}^{-2}$.

At large projected radii, each LAE shows an extended profile, which can be identified as the diffuse LAH. The profile at large radii is much flatter than the central part. The surface brightness level of this extended component displays a substantial variation among the nine individual LAEs, as large as two orders of magnitude.

In the right panel of Figure 3, we compare the overall mean profile of the nine model LAEs with the one derived by Momose et al. (2014) from stacking the Ly α images of 316 $z \sim 3.1$ LAEs. According to Momose et al. (2014), the data at $R \lesssim 40$ kpc are reliable, while at larger radii systematic effects in the stacking analysis become significant compared to the signal (see the top-middle panel in their Figure 8). We mark such a transition by using filled circles at $R \lesssim 40$ kpc and open circles at $R \gtrsim 40$ kpc for the data points. The shaded region around the mean model profile quantifies the uncertainty. The upper (lower) boundary is derived by excluding the LAE with the lowest (highest) surface brightness and averaging over the other eight LAEs. This serves to only provide some rough idea on the variation level of the mean profile, given the small number of model LAEs in our analysis.

On small scales ($R \lesssim 15$ kpc), the model profile matches the observed profile extremely well, which is striking. At first glance one may attribute this to coincidence, since we do not intend to fit the observed profile and we do not have any free parameters to adjust in our model. We directly use the Ly α emissivity and gas distribution in the simulation. The only two changes we apply in the model besides the radiative transfer calculation are “effective” dust and IGM absorption. The

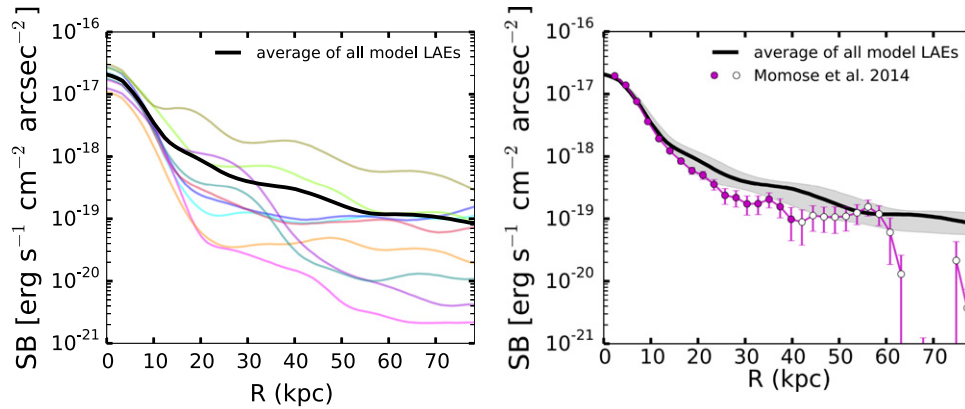


Figure 3. $\text{Ly}\alpha$ surface brightness profiles for the model LAEs in our analysis. Left: $\text{Ly}\alpha$ surface brightness profiles for individual model LAEs, with the average over all nine LAEs shown as the black curve. While the nine LAEs have similar surface brightness levels at small radii, they display large variations at large radii, reflecting the differences in gas distributions in our model halos. Right: comparison of the average $\text{Ly}\alpha$ profile with observational results in Momose et al. (2014). Beyond ~ 40 kpc systematic effects in the image stacking analysis become important, indicated by the open circles. The shaded region gives an idea of the spread in the model profile, obtained by excluding the LAE with the faintest or the brightest extended profiles from the average.

“effective” $\text{Ly}\alpha$ extinction optical depth is the same as the one adopted in Cen & Zheng (2013) for studying LABs, which suppresses the initial intrinsic $\text{Ly}\alpha$ emission. It aims at accounting for any uncertainties in the galaxy formation simulation. We tie it to the SFR and the relation is fixed by considering halos above $10^{12} M_{\odot}$ in Cen & Zheng (2013). We apply a mean absorption (scattering) for $\text{Ly}\alpha$ photons escaping the grid from the IGM outside of the simulation box.

In Cen & Zheng (2013), the observed $\text{Ly}\alpha$ luminosity–size relation of LABs and the $\text{Ly}\alpha$ luminosity function of LABs are reproduced by our radiative transfer modeling. So it may not be too surprising that the similar model also provides a good match to the $\text{Ly}\alpha$ emission in lower mass halos ($10^{11.5} M_{\odot}$). Since the surface brightness profile at the central part is largely determined by the PSF, the agreement with the observation means that the central $\text{Ly}\alpha$ luminosity in our model happens to be similar to the average luminosity of the 316 LAEs in the stacking analysis in Momose et al. (2014), which by all means is an encouraging sign.

At larger radii ($R \gtrsim 15$ kpc), the model curve is slightly higher (at a factor of 2 level) than the observation. Given the small number of LAEs and the lack of adjustment in the model, the agreement to the observation still appears remarkable, in particular if the uncertainties in the data points and in the model curve are taken into account (keeping in mind that the data may suffer from significant systematic bias at $R \gtrsim 40$ kpc). Both the shape and extent of the LAH are reasonably reproduced.

As a whole, our model mean $\text{Ly}\alpha$ surface brightness profile, effectively computed from stacking $\text{Ly}\alpha$ images of nine LAEs viewed along many different directions, shows good agreement with stacking analysis from observed $z \sim 3.1$ LAEs, from the central part to the diffuse LAH extended to $R \sim 60$ kpc. However, the systematic effect in the data analysis makes the comparison beyond ~ 40 kpc less reliable, and the apparent disagreement at $R \gtrsim 60$ kpc is not significant. We proceed to investigate the contributions from various components to the surface brightness profile to gain more insights.

3.2. Decomposing the $\text{Ly}\alpha$ Surface Brightness Profile

We record the initial position of each photon, which makes it possible to separate the contributions to the surface brightness

profile from photons originating at different places in our simulation.

In each halo, there is a central LAE with strong $\text{Ly}\alpha$ emission. We attribute $\text{Ly}\alpha$ photons launched within 10 kpc of the halo center to the central LAE. There are also a few regions in the halo with high $\text{Ly}\alpha$ emissivity, which are small star-forming galaxies around the central LAE. In the $\text{Ly}\alpha$ images shown in Figure 2, such regions appear as relatively isolated peaks with surface brightness above $\sim 10^{-19} \text{ erg s}^{-1} \text{ cm}^{-2} \text{ arcsec}^{-2}$. The majority of them are below the detection threshold for typical LAE surveys, as is the case in Momose et al. (2014). In three of the nine LAEs, a few of the high emissivity regions can reach the detection threshold, and would show up as isolated LAEs around the central LAEs. We refer to the high emissivity regions as “knots” and associate to each knot $\text{Ly}\alpha$ photons launched within 10 kpc of its center. Photons that belong to neither the central LAE nor the knots are identified as being emitted from the background of the simulation box. Most of them come from small clumps of gas that possess low rates of star formation. Clearly the distinction between the knots and the background depends on our choice, which can be arbitrary. However, our separation here serves the purpose of obtaining a rough idea on how $\text{Ly}\alpha$ photons from different physical regions contribute to the surface brightness profile.

The left panel of Figure 4 shows the decomposition of the mean surface brightness profile (black) into contributions from $\text{Ly}\alpha$ photons originating in the central LAE (red), the knots regions (blue), and the background regions (green).

After the radiative transfer, $\text{Ly}\alpha$ photons originating from the central LAE appear to peak around the central region, following the PSF. The entire amplitude of the overall surface brightness profile at $R < 10$ kpc comes from this component. The scatterings of photons with neutral hydrogen atoms in the circumgalactic and intergalactic media lead to an extended profile beyond ~ 15 kpc. The profile drops toward large radii, roughly following $R^{-3.3}$, which is too steep to account for the LAHs seen in both the model and observations.

$\text{Ly}\alpha$ photons from the knots and background regions make comparable contributions (within a factor of about 2) to the overall surface brightness profile at scales above ~ 20 kpc. They have similar profiles, which in turn are similar to that of the LAH and are flatter than the extended profile from scattered

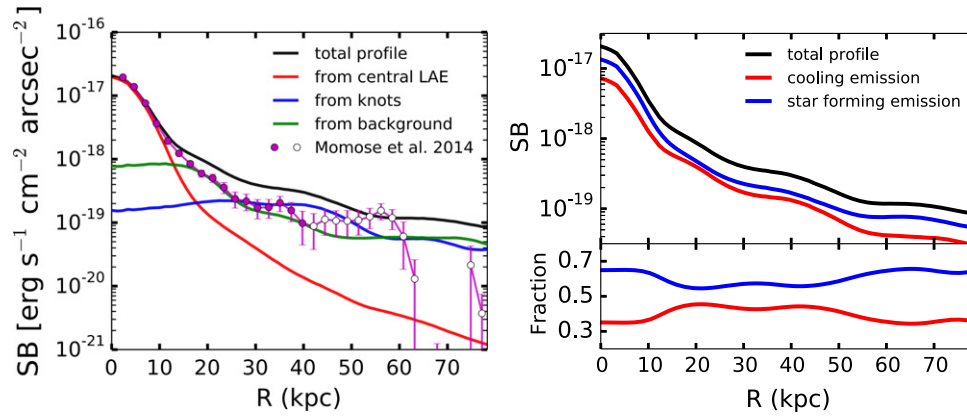


Figure 4. Decomposition of the total $\text{Ly}\alpha$ surface brightness profile into different components of $\text{Ly}\alpha$ emission. Left: the decomposition of the total profile into contributions from the central LAE (red curve), other high emission knots (blue curve), and background regions (green curve). Observational data from Momose et al. (2014) is shown in purple. Systematic bias is important for $R \gtrsim 40$ kpc, indicated by the open circles. Note that at radii larger than ~ 10 kpc, the profile from the central LAE is unable to account for observations, with the knot and background profiles playing dominant roles. Right: the decomposition of the total profile into contributions from star formation and cooling emission. The top panel shows profiles for each emission type, given in surface brightness units of $\text{erg s}^{-1} \text{cm}^{-2} \text{arcsec}^{-2}$. Star-forming emission is shown in blue, and cooling emission is shown in red. The bottom panel shows the fractional contribution that each emission type makes to the total profile.

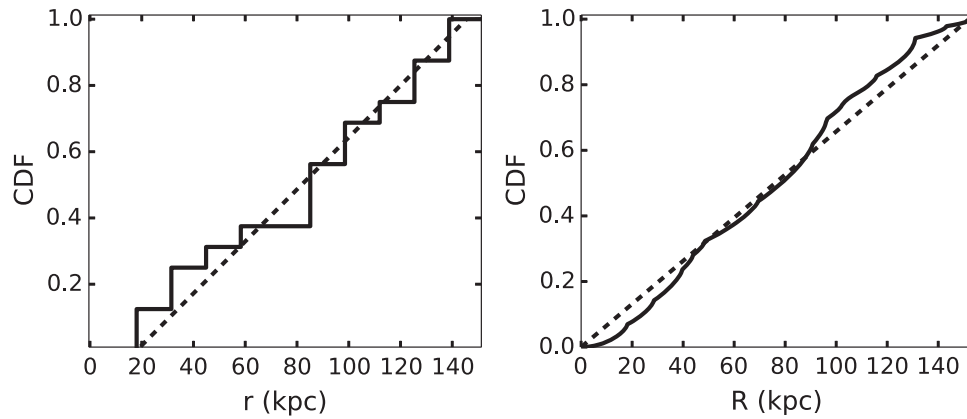


Figure 5. Spatial distribution of the identified high emission knots in our simulation. Left: the distribution of 3D distances of the knots to the box center. The solid line shows a cumulative distribution function (CDF) of the 3D distances, with the dashed curve corresponding to a number density profile $n(r) = 0$ for $r < 20$ kpc and $n(r) \propto r^{-2}$ for $r \geq 20$ kpc. Right: the distribution of 2D projected distances of the knots to the box center. The solid line shows the CDF of the 2D distances and the dashed curve is for a number density distribution $\propto R^{-1}$.

photons from the central LAE. Together, they dominate the profile at $R \gtrsim 20$ kpc.

The above decomposition leads to the interesting implication that the observed extended $\text{Ly}\alpha$ emission of LAHs is largely caused by emission from regions of low SFRs spatially distributed inside the host dark matter halos of the central LAEs, and that photons diffusing out from the central LAE as a result of the radiative transfer process play only a secondary role in producing the observed extended emission.

We also decompose the surface brightness profile into contributions from $\text{Ly}\alpha$ photons generated by star formation and cooling radiation, as shown in the right panel of Figure 4. The profiles from the two contributions are similar, but the photons from cooling radiation always sub-dominate, making about 30%–40% of the total $\text{Ly}\alpha$ light in the extended LAHs.

Because the identified high-emission knots contribute significantly to the surface brightness profile at large radii, it is important to examine their spatial distribution. The left panel of Figure 5 shows the cumulative distribution function (CDF) of the 3D distance r from the knots to the center for all the nine LAEs. Since we define the radius of each knot region and the central LAE to be 10 kpc, any high-emission areas within

20 kpc of the center will not be identified as independent knots in our analysis. Therefore, the CDF curve starts at $r = 20$ kpc. The dashed curve corresponds to a number density distribution $n(r) \propto r^{-2}$ (for $r \geq 20$ kpc and 0 for $r < 20$ kpc). The plot shows that the high-emission knots closely follow a singular isothermal distribution up to at least $\sim 3R_{\text{vir}}$.

As we study the surface brightness profile, it would be more illustrative to examine the projected distribution of the knots. For this purpose, we chose a large number of isotropically distributed viewing directions. For each viewing direction and each LAE, we record the projected radius to the center for each knot. The right panel of Figure 5 shows the CDF for the 2D projected radii R . The dashed curve is the CDF for a surface number density that follows R^{-1} , which appears to be a reasonable description of the distribution of knots. This is consistent with the CDF of the 3D radii. The distribution of knots explains the shallow slope in the mean surface brightness profile seen in the model or observed LAHs (e.g., Figures 3 and 4), which has a slope around -1 .

Figure 6 shows the decomposition of our surface brightness profiles into contributions from star formation and cooling radiation for the central LAE, the identified knot regions, and

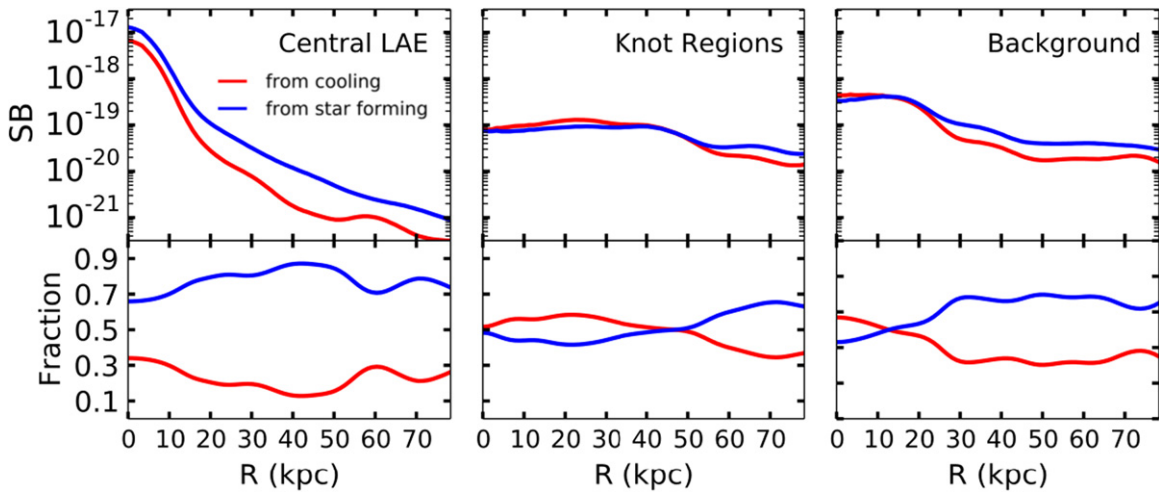


Figure 6. A further decomposition of the averaged surface brightness profile into contributions from star formation (blue curves) and cooling radiation (red curves). From left to right, the panels show profiles for photons produced within 10 kpc of the central LAEs, within the knot regions, and from the background areas. The top panels show surface brightness in units of $\text{erg s}^{-1} \text{cm}^{-2} \text{arcsec}^{-2}$, while the bottom panels show the relative contributions.

the background. For $\text{Ly}\alpha$ photons produced in the central LAE, cooling radiation makes up about 1/3 of the observed $\text{Ly}\alpha$ emission near the center, and its contribution drops to 15% at $R \sim 40$ kpc. For $\text{Ly}\alpha$ photons produced in the knot regions, cooling radiation and star formation contributions are comparable, and for those produced in background, the star formation contribution dominates. The latter two components depend on how we define knot regions. If we choose a lower threshold to define knots, star formation would become the dominant mechanism in producing $\text{Ly}\alpha$ photons in knot regions.

3.3. Possible Constraints from the UV Surface Brightness Profile

The $\text{Ly}\alpha$ surface brightness profile from our model shows an encouraging agreement with the data. Besides $\text{Ly}\alpha$, the stacking analysis is also performed for UV images (e.g., Momose et al. 2014). UV photons are produced from star formation. Unlike $\text{Ly}\alpha$ photons, they do not interact with neutral hydrogen through resonant scattering. Instead, they escape directly from their point of creation (modulated by dust extinction), which allows them to serve as a tool to map out regions of star formation. The UV profile of LAEs can therefore provide complementary information about LAHs and can be used to further constrain the origin of LAHs.

We convert the SFR to UV luminosity (at rest-frame 1500 Å) using the prescription $L_{\text{UV}} = 8 \times 10^{27} [\text{SFR} / (M_{\odot} \text{yr}^{-1})] \text{erg s}^{-1} \text{Hz}^{-1}$ (Madau et al. 1998). It assumes a Salpeter initial mass function (IMF) of stars and solar metallicity.

While dust extinction should also be included to obtain the observed UV luminosity, it is degenerated with the above assumption about the stellar population and to a less degree with the star formation history. For example, a sub-solar metallicity (or a different IMF, e.g., Chabrier IMF) results in a higher SFR-to-UV conversion factor, and the combined effect of the metallicity and IMF can lead to a factor of a few increase in the conversion (e.g., Leitherer et al. 1999; Madau & Dickinson 2014). The dust extinction works in the direction to bring the conversion factor toward the above value. Given such uncertainties in the model, we can simply adopt the above

conversion to proceed, and rescale the model UV profile if necessary to fit the observed profile.

We create UV photons based on the SFR in each cell and assign a random escape direction for each photon. Figure 7 displays the UV images of the nine model galaxies observed along the same direction as in Figure 2. To study the average UV light distribution seen in the stacking analysis, we follow the method described in Section 2.2 to produce the average UV surface brightness profile for each model LAE.

The black curve in the left panel of Figure 8 shows the UV profile predicted by our model. At small radii ($R \lesssim 15$ kpc), the model curve is almost right on top of the observed profile.

Such a coincidence indicates that our SFR-to-UV conversion factor is about right in reflecting a combined effect of stellar population, metallicity, extinction, and model SFR, even though there are uncertainties in each component and the overall model is approximate. As such, we make no adjustments to our initial conversion factor.

The model reproduces the central UV luminosity, and the shape of the profile simply follows that of the PSF.

At large radii ($R \gtrsim 15$ kpc), our model shows an extended UV halo (left panel of Figure 8). This is not unexpected, given that emission produced from star formation in the outer halo makes a substantial contribution to the extended $\text{Ly}\alpha$ profile (Figure 6). The model UV profile is in apparent tension with observations (Momose et al. 2014), where little evidence is shown for such extended UV halos (see the data points in the left panel of Figure 8).

We note that there are some residuals of sky subtraction found in the composite UV images of Momose et al. (2014). To quantify the significance of the apparent tension between the model and observation, we evaluate the sky subtraction systematics in the average UV surface brightness profile. We find that there is a signal of sky over-subtraction at the surface brightness level of $3.0 \times 10^{-33} \text{erg s}^{-1} \text{cm}^{-2} \text{Hz}^{-1} \text{arcsec}^{-2}$, corresponding to a maximum negative value of the UV surface brightness estimate of the LAH (R. Momose et al. 2015, in preparation). Therefore, we conclude that the average UV profile below the above level is subject to the influence of the systematics. Note that the effect of sky over-subtraction systematics is canceled out in the $\text{Ly}\alpha$ surface brightness

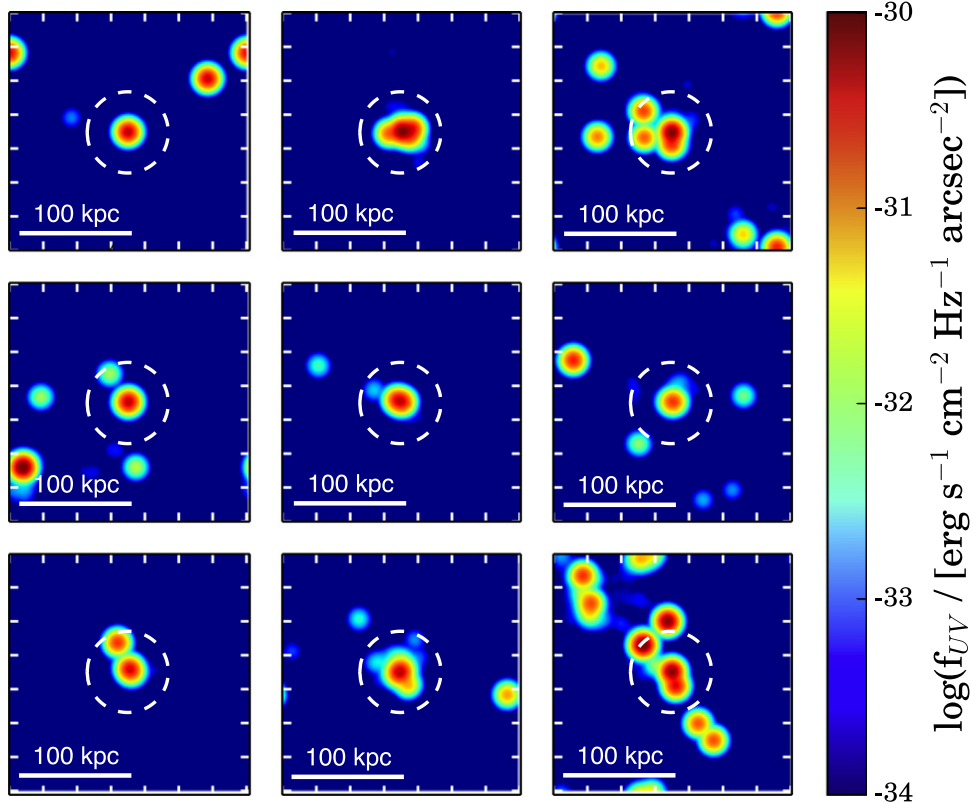


Figure 7. UV surface brightness images for all nine model LAEs in our original analysis. Each image is 224 kpc (physical) on a side and has been smoothed by a 2D Gaussian kernel with a FWHM of $1''.32$ to match observations. The dashed circle in each panel has a radius of 40 kpc, roughly corresponding to the radius that systematic effects become important in the stacking analysis in Momose et al. (2014). The observed profile can potentially be used to put constraints on the clustered UV sources around the central galaxies, as discussed in the text.

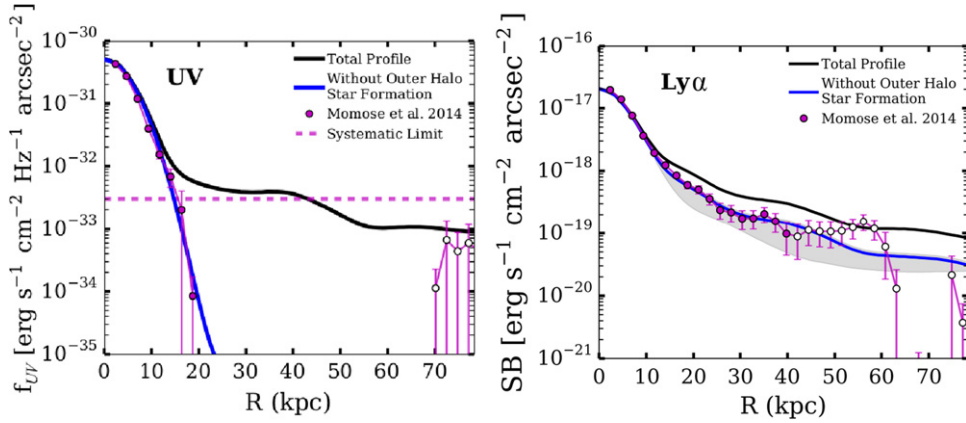


Figure 8. Average UV and $\text{Ly}\alpha$ surface brightness profiles and the effect of star formation in the outer halo. In each panel, observational data are taken from Momose et al. (2014) with open circles representing the region where the data starts to be limited by systematics. Left: comparison of our UV profiles with observational data. The black curve is the average profile from our initial model. The blue curve shows the effect of removing star formation in the outer halo, keeping only the star-forming emission from the central LAE. The dashed line is drawn at $3.0 \times 10^{-33} \text{ erg s}^{-1} \text{ cm}^{-2} \text{ Hz}^{-1} \text{ arcsec}^{-2}$, which is the level of systematic effects in the image stacking analysis (see the text). This line represents an upper limit for any extended UV emission that actually occurs. Right: the corresponding changes in the model $\text{Ly}\alpha$ profile. The black curve shows our total $\text{Ly}\alpha$ profile, and the blue curve shows the effect of removing star formation emission from the outer halo. The gray shaded region in the right panel gives an idea of the spread of the profile, obtained by excluding the LAE with the faintest or the brightest extended profiles from the average.

profile of the LAH, because the $\text{Ly}\alpha$ profile is obtained by taking the difference of the composite broadband and narrowband images, which have the same level of sky over-subtraction.

The dashed line in the left panel of Figure 8 shows the sky-subtraction systematic effect at the surface brightness level of $3.0 \times 10^{-33} \text{ erg s}^{-1} \text{ cm}^{-2} \text{ Hz}^{-1} \text{ arcsec}^{-2}$, which can be regarded

as an upper bound for extended UV profile. Our model UV profile (black curve) appears to be at a similar level. Therefore, by accounting for the systematics in the data, no significant tension is found between the model and the observation. Given the sky-subtraction systematics, the UV profile obtained in Momose et al. (2014; data points in the left panel of our Figure 8) represents a lower bound, which essentially follows

the PSF and is determined by the central star formation. To match this case, we construct a modified model by removing star formation in the outer halo regions in our model. It is not surprising to see that the modified model profile produced in this way (blue curve in the left panel of Figure 8) follows the PSF, as with the data points.

The default model profile (black curve) and the modified one (blue curve) should be able to bracket all possible cases of the extended UV profile. Improved measurements of the UV profile with well-controlled systematics would provide important information on the amount of star formation in the outer halo. This in turn would improve our understanding of the origin of the extended LAH, along with its partition into contributions from star formation and cooling radiation. With the current situation, the above two boundary cases allow us to infer the range of the relative contributions of star formation and cooling radiation to the Ly α surface brightness profile.

The black curve in the right panel of Figure 8 corresponds to the Ly α profile from our default model. We find that the total Ly α luminosity within the projected radius $R < R_{\text{vir}} = 56$ kpc can be broken down into the following contributions: 33% from star-forming photons produced in the central galaxy, 15% from cooling radiation emitted from the central galaxy ($r < 10$ kpc), 28% from star-forming photons produced in the outer halo, and 25% from cooling radiation in the outer halo. In the extended part of the profile (defined as emission observed at $15 \text{ kpc} \lesssim R \lesssim 56 \text{ kpc}$), the fraction of photons from cooling radiation is about 42%.

The Ly α profile after removing star formation from the outer halo is shown as the blue curve in the right panel of Figure 8. The effect is not drastic, and the Ly α profile for this case drops to a level in even better agreement with observations. For this modified profile, the average component contributions to the total Ly α luminosity within projected radius $R < R_{\text{vir}} = 56$ kpc are 45% from star-forming photons produced in the central galaxy, 20% from cooling radiation within and around the central galaxy ($r < 10$ kpc), and 35% from cooling radiation in the outer halo. On average, cooling radiation can now contribute to about half of the total Ly α luminosity. If we focus on the extended part of the profile ($15 \text{ kpc} \lesssim R \lesssim 56 \text{ kpc}$), the fraction of the cooling radiation contribution is about 75%. With this prescription, the extended LAH is dominated by cooling radiation.

Although the best currently available data is limited by systematics, the UV profile in combination with the Ly α profile can help to constrain the nature of LAHs. Our investigation implies that cooling radiation in the outer halo may play a significant role in forming extended LAHs (e.g., contributing more than half of the emission), a prediction that can be tested with tighter observational constraints on the UV profile. The caveats and more discussions are presented in the next section.

4. SUMMARY AND DISCUSSION

We perform Ly α radiative transfer modeling of $z = 3.1$ LAEs with a high resolution hydrodynamic cosmological galaxy formation simulation to study the extended Ly α -emitting halos recently discovered in observation from image stacking analysis. We develop a method to compute the mean surface brightness profile from averaging over many different viewing directions. We consider nine model LAEs residing in halos of $10^{11.5} M_{\odot}$ and find their mean Ly α surface brightness

profile to be in remarkable agreement with the observed profile in Momose et al. (2014), at both the central and extended parts.

To investigate the origin of the extended Ly α emission, we decompose the profile into contributions from Ly α photons produced in different regions, which include the central LAE in each simulation box, dense regions of high star formation activity spatially separated from the central LAE (dubbed as “knots”), and faint background areas. The latter two outer halo components are associated with satellite galaxies or tidally stripped materials in the halo.

Ly α photons originating near the halo center (from both star formation and cooling radiation) but scattered to large radii by the hydrogen atoms in the CGM do produce an extended LAH, as predicted by, e.g., Laursen & Sommer-Larsen (2007)⁵ and Zheng et al. (2011b). However, our radiative transfer model with the high-resolution galaxy formation simulation shows that such a contribution alone is not able to explain the surface brightness level of the observed LAH (e.g., lower by a factor of 10 around $R = 40$ kpc). Instead, the extended LAH is dominated by emission from the knots and the background regions of the outer halo. The result implies that scattering of Ly α photons from bright, central sources is less important in forming LAHs than previously thought.

Certainly the exact profile created by the scattered, centrally produced photons should depend on the density and velocity distribution of the circumgalactic gas. Some analytic models with clumpy CGM and decelerating outflows can produce scattered LAHs at the observed surface brightness level (e.g., Steidel et al. 2011; Dijkstra & Kramer 2012). It is worth investigating the contribution from such scattered halos with more realistic CGM distributions from high-resolution galaxy formation simulations with various prescriptions of the star formation feedback (e.g., Kimm et al. 2015; Muratov et al. 2015; Suresh et al. 2015). By performing a test with a lower-resolution grid used in the radiative transfer calculation, we also find that the scattered profile shows a weak dependence on the resolution, becoming slightly more extended with higher resolution. However, in both cases the scattered profile drops rapidly toward large radii, remaining unlikely to account for the observed one.

Ly α emission from the outer halo has two components—gravitational cooling radiation and emission from star formation. In the simulation, we find that star formation slightly dominates, and cooling radiation makes a substantial contribution. Our model predicts the existence of an extended UV halo at a brightness level of $\sim 3 \times 10^{-33} \text{ erg s}^{-1} \text{ cm}^{-2} \text{ Hz}^{-1} \text{ arcsec}^{-2}$, which is right at the limit of the sky-subtraction systematics in observational data (Momose et al. 2014). If actual UV halos (from improved data analysis) are significantly dimmer than this, we will need to investigate how to suppress the UV profile in the model (e.g., identifying the likely cause in the simulation for the over-prediction of star formation in the outer halo or studying the dust attenuation effect in the outer halo). Although the best currently available UV profile measurement does not serve as a robust constraint as a result of systematics, we find that the extended Ly α profile becomes even better reproduced after removing star formation in the outer halo in order to suppress the UV profile.

Taken at face value, our investigation shows that our initial model can explain both the observed Ly α and UV profiles of

⁵ Cooling radiation in the outer halo is also included in Laursen & Sommer-Larsen (2007). However, there is no discussion on its contribution to the LAH for an obvious reason—LAHs had not yet been discovered in observations.

LAEs in Momose et al. (2014), from small radii ($\lesssim 15$ kpc) to large radii (up to ~ 80 kpc). The agreements between the model and data are excellent. This is remarkable, especially given that we do not intend to fit the profiles by tuning parameters. Depending on the accuracy of our star-forming recipe and the loose constraints from the UV halo, we find that cooling radiation can contribute 40%–55% of the total Ly α luminosity within projected radius $R < R_{\text{vir}}$, where $R_{\text{vir}} = 56$ kpc ($\sim 7''2$) is the virial radius of the LAE host halo. For the diffuse LAH, which is usually buried in sky noise for individual LAEs, the contribution from cooling radiation is more substantial, making up about 42%–75% (within $15 \text{ kpc} \lesssim R \lesssim 56 \text{ kpc}$).

Gravitational cooling radiation from accretion of gas is a process expected to occur during galaxy formation, mainly in the form of Ly α emission from collisional excitation and de-excitation of hydrogen atoms in gas around 2×10^4 K (e.g., Fardal et al. 2001). Many previous studies of cooling radiation with analytic calculations and hydrodynamical simulations focus on investigating it as a possible mechanism to explain LABs (e.g., Haiman et al. 2000; Fardal et al. 2001; Furlanetto et al. 2005; Yang et al. 2006; Dijkstra & Loeb 2009; Faucher-Giguère et al. 2010; Goerdt et al. 2010), which are more luminous than LAHs (Steidel et al. 2000). As shown by Yang et al. (2006) and Faucher-Giguère et al. (2010), an accurate prediction of the cooling Ly α emission relies on an accurate treatment of the self-shielding effect for the ionizing photons, which affects the ionization and thermal states of the accreted gas. In the simulation used in this work, self-shielding correction is performed on-the-fly. There could be small variations in the predicted cooling radiation with different self-shielding correction methods, but it is unlikely to remove the cooling radiation signal in our model, which is significant regardless of the accuracy of our star-forming recipe.

One caveat to keep in mind is that our results in this paper are based on radiative transfer modeling of nine simulated galaxies in halos of $10^{11.5} M_{\odot}$. First, our analysis suffers from small number statistics. While we attempt to make full use of the nine galaxies by obtaining the mean surface brightness profile from averaging all viewing angles (effectively creating a much larger sample for stacking), modeling more galaxies definitely helps the study of LAHs. More galaxies are also needed to explore the dependence of LAHs on the properties of galaxies and their environments (e.g., Matsuda et al. 2012). Second, the mass of halos ($10^{11.5} M_{\odot}$) considered in this work seems to be on the high end of LAE-hosting halos. The LAE halo masses inferred from clustering analysis are typically $10^{11 \pm 1} M_{\odot}$ (Ouchi et al. 2010). Clearly it is necessary to investigate how the Ly α and UV surface brightness profiles and their decomposition into cooling and star-forming components vary with halo mass, and to make comparisons with data especially as better observational constraints on the UV profile become available. As an example of the potential impact of halo mass, Rosdahl & Blaizot (2012) find that the extent of cooling radiation in the outer halo is dependent on halo mass, resulting from a positive correlation between the efficiency of cold streaming accretion and halo mass. Additional radiative transfer modeling of galaxies in lower mass halos comparing emission from the central LAE with star formation and cooling radiation in the outer halo will elucidate to what extent our results in this paper hold.

We plan to carry out studies related to the above aspects and the redshift evolution of LAHs for a better understanding of the

origin and for using LAHs to learn about the CGM and galaxy formation.

We thank the anonymous referee for constructive comments and Mark Dijkstra for helpful discussions. E.L., Z.Z., and R.S. are supported by NASA grant NNX14AC89G and NSF grant AST-1208891. The support and resources from the Center for High Performance Computing at the University of Utah are gratefully acknowledged. Computing resources were in part provided by the NASA High-End Computing (HEC) Program through the NASA Advanced Supercomputing (NAS) Division at Ames Research Center. R.C. is supported in part by grants NASA NNX11AI23G and NNX12AF91G. This work was supported by World Premier International Research Center Initiative (WPI Initiative), MEXT, Japan, and KAKENHI (23244025) Grant-in-Aid for Scientific Research (A) through Japan Society for the Promotion of Science (JSPS).

REFERENCES

- Barnes, L. A., & Haehnelt, M. G. 2010, *MNRAS*, **403**, 870
 Barnes, L. A., Haehnelt, M. G., Tescari, E., & Viel, M. 2011, *MNRAS*, **416**, 1723
 Brinchmann, J., Charlot, S., White, S. D. M., et al. 2004, *MNRAS*, **351**, 1151
 Bryan, G. L., & Norman, M. L. 2000, *IMA*, **117**, 165
 Cen, R. 2011, *ApJL*, **742**, L33
 Cen, R. 2012, *ApJ*, **748**, 121
 Cen, R., & Zheng, Z. 2013, *ApJ*, **775**, 112
 Dijkstra, M., & Kramer, R. 2012, *MNRAS*, **424**, 1672
 Dijkstra, M., & Loeb, A. 2009, *MNRAS*, **400**, 1109
 Fardal, M. A., Katz, N., Gardner, J. P., et al. 2001, *ApJ*, **562**, 605
 Faucher-Giguère, C.-A., Kereš, D., Dijkstra, M., Hernquist, L., & Zaldarriaga, M. 2010, *ApJ*, **725**, 633
 Feldmeier, J. J., Hagen, A., Ciardullo, R., et al. 2013, *ApJ*, **776**, 75
 Furlanetto, S. R., Schaye, J., Springel, V., & Hernquist, L. 2005, *ApJ*, **622**, 7
 Fynbo, J. P. U., Ledoux, C., Möller, P., Thomsen, B., & Burud, I. 2003, *A&A*, **407**, 147
 Gawiser, E., Francke, H., Lai, K., et al. 2007, *ApJ*, **671**, 278
 Goerdt, T., Dekel, A., Sternberg, A., et al. 2010, *MNRAS*, **407**, 613
 Guaita, L., Gawiser, E., Padilla, N., et al. 2010, *ApJ*, **714**, 255
 Haiman, Z., Spaans, M., & Quataert, E. 2000, *ApJL*, **537**, L5
 Jeon-Daniel, A., Ciardi, B., Maio, U., et al. 2012, *MNRAS*, **424**, 2193
 Jiang, L., Egami, E., Fan, X., et al. 2013, *ApJ*, **773**, 153
 Joung, M. R., Cen, R., & Bryan, G. L. 2009, *ApJL*, **692**, L1
 Kimm, T., Cen, R., Devriendt, J., Dubois, Y., & Slyz, A. 2015, *arXiv:1501.05655*
 Laursen, P., & Sommer-Larsen, J. 2007, *ApJL*, **657**, L69
 Laursen, P., Sommer-Larsen, J., & Andersen, A. C. 2009, *ApJ*, **704**, 1640
 Leitherer, C., Schaerer, D., Goldader, J. D., et al. 1999, *ApJS*, **123**, 3
 Madau, P., & Dickinson, M. 2014, *ARA&A*, **52**, 415
 Madau, P., Pozzetti, L., & Dickinson, M. 1998, *ApJ*, **498**, 106
 Matsuda, Y., Yamada, T., Hayashino, T., et al. 2012, *MNRAS*, **425**, 878
 Momose, R., Ouchi, M., Nakajima, K., et al. 2014, *MNRAS*, **442**, 110
 Muratov, A. L., Keres, D., Faucher-Giguère, C.-A., et al. 2015, *arXiv:1501.03155*
 Ouchi, M., Shimasaku, K., Akiyama, M., et al. 2008, *ApJS*, **176**, 301
 Ouchi, M., Shimasaku, K., Furusawa, H., et al. 2010, *ApJ*, **723**, 869
 Partridge, R. B., & Peebles, P. J. E. 1967, *ApJ*, **147**, 868
 Rhoads, J. E., Dey, A., Malhotra, S., et al. 2003, *AJ*, **125**, 1006
 Rosdahl, J., & Blaizot, J. 2012, *MNRAS*, **423**, 344
 Steidel, C. C., Adelberger, K. L., Shapley, A. E., et al. 2000, *ApJ*, **532**, 170
 Steidel, C. C., Bogosavljević, M., Shapley, A. E., et al. 2011, *ApJ*, **736**, 160
 Suresh, J., Bird, S., Vogelsberger, M., et al. 2015, *MNRAS*, **448**, 895
 Tasitomi, A. 2006, *ApJ*, **645**, 792
 Yang, Y., Zabludoff, A. I., Davé, R., et al. 2006, *ApJ*, **640**, 539
 Zahid, H. J., Yates, R. M., Kewley, L. J., & Kudritzki, R. P. 2013, *ApJ*, **763**, 92
 Zheng, Z., Cen, R., Trac, H., & Miralda-Escudé, J. 2010, *ApJ*, **716**, 574
 Zheng, Z., Cen, R., Trac, H., & Miralda-Escudé, J. 2011a, *ApJ*, **726**, 38
 Zheng, Z., Cen, R., Weinberg, D., Trac, H., & Miralda-Escudé, J. 2011b, *ApJ*, **739**, 62
 Zheng, Z., & Miralda-Escudé, J. 2002, *ApJ*, **578**, 33
 Zheng, Z., & Wallace, J. 2014, *ApJ*, **794**, 116